Engineering Research Express

PAPER

Development of unsteady multi-hole pressure probes based on fiber-optic pressure sensors

Florian M Heckmeier[1] , Daniel Iglesias[2], Stefanie Kreft[3], Sascha Kienitz[3] and Christian Breitsamter[1]

[1] Chair of Aerodynamics and Fluid Mechanics, Department of Mechanical Engineering, Technical University of Munich, 85748 Garching bei München, Germany
[2] Vectoflow GmbH, 82205 Gilching, Germany
[3] Fos4X GmbH, 81371 Munich, Germany

E-mail: florian.heckmeier@aer.mw.tum.de

Abstract

For measurements of unsteady flow phenomena with multi-hole pressure probes, pressure transducers are integrated in the probe near the probe tip. The application of additive manufacturing enables a wide variation in probe geometries for complex use cases. The spatial characteristics of the unsteady probe are determined by the steady state calibration in a known free-jet wind tunnel. Furthermore, the acoustic/pneumatic line-cavity system, that emerges inside the channels of the probe, is investigated in detail in the temporal calibration. In order to realize multi-hole probes with higher temporal resolution, which can be operated in harsh environments, a fiber-optic pressure sensor is developed. The measurement principle of the fiber-optic sensor is based on the Fabry-Pérot interferometer effect. The sensor is operated differentially with a pressure capillary by either pressurizing the sensor or using the surrounding static pressure as the reference pressure. Besides calibration of the sensor, comparisons with a state-of-the-art piezo-resistive pressure transducer have been performed. The focus of this work is on the reproducibility of both frequency response and amplitude.

1. Introduction

Highly fluctuating flow fields are caused for example by interactions of rotating and non-rotating components in turbo machines. Sources of unsteadiness, like rotor-stator interaction, secondary flows or blade wake shedding, have to be understood either by means of numerical simulations or measurements. Even though the development and optimization of computational fluid dynamics (CFD) simulations enables the unsteady flow patterns to be handled numerically, experimentally gained data are still of interest for academic and industrial research. The reason why experiments can be still justified alongside numerical simulations is twofold: firstly, experimental results often serve as a database for the validation for CFD solutions. Secondly, live monitoring of machines (e.g. turbines in operation) is only possible experimentally. Certain requirements have to be met by probes for unsteady flow measurement in turbomachines. This ensures that all sources of unsteadiness can be resolved precisely. For example, bandwidths corresponding to blade passing frequencies of up to $f = 10$ kHz are the benchmark for the temporal resolution. For aerodynamic measurements of flow fields, measurement techniques can basically be divided into non-intrusive/optical and intrusive techniques. Particle image velocimetry (PIV) and laser Doppler anemometry (LDA) are the main representatives of optical measurements, which are used to examine the velocity field. However, in some cases they are disadvantageous because of high calibration efforts and significant set up costs. Furthermore, the need for optical access in the test section rules out optical measurement techniques in various test situations. Of the intrusive measuring methods, hot-wire probes and multi-hole pressure probes are most commonly used. On the one hand, hot-wire anemometry is characterized by its high temporal resolution. On the other hand, hot-wires lack of mechanical robustness when being set in harsh environments. In contrast, multi-hole pressure probes are cost-efficient and easy to use. Since

the 1990s research institutes worldwide developed multi-hole pressure probes for unsteady measurements, so-called fast-response aerodynamic probes (FRAP). Ainsworth *et al* [1] describe the application of piezo-resistive silicon pressure sensors for unsteady measurements in turbomachines. Different designs of unsteady pressure probes, for example with respect to their shape, are discussed in [2]. The use in environments with high temperatures, varying pressure ranges or spatial restrictions of the installation space, require various design, assembly and calibration strategies. Meaningful and accurate measurement results can only be achieved if the probe is calibrated in representative conditions. Similarities in Reynolds number *Re* and Mach number *Ma* as well as dynamic similarity have to be ensured during calibration and experiments. Several design trends can be observed in the literature. Especially sensor specific limitations or limits due to thermal durability are the main drivers for changes in probe design. Unsteady pressure probes can be divided into real or virtual multi-sensor probes. Virtual probes use the periodicity of turbomachinery flows and are yawed to virtually simulate a multi-sensor probe [3]. Gossweiler *et al* [4] developed single-sensor cylinder probes for turbomachinery measurements and placed micro-electro-mechanical system (MEMS) sensors in the probe tip. Humm *et al* [5] studied various probe shapes and geometric parameters regarding their intrusive influence in flow fields. Further investigations based on the two aforementioned studies show the application of a fast-response cylinder probe in a centrifugal compressor [6–8]. Moreover, Rediniotis *et al* [9] built a MEMS based fast-response five sensor probe for subsonic measurements, in order to test the angular/spatial and temporal characteristics of the probe with signal frequencies of up to 400 Hz. A flush-mounted sensor experiences high loads, which can be reduced by placing the sensor farther inside the probe. However, by doing so, a characterization of the acoustic line-cavity system in the pressure channels is needed. A reconstruction procedure of the unknown flow parameters at the probe tip is introduced for a five-hole probe in [10]. Persico *et al* [11] developed cylindrical pressure probes and calibrated the pneumatic line-cavity system inside the probe in a low-pressure shock-tube. Sieverding *et al* [12] and Brouckaert [13] developed single- and multi-sensor unsteady pressure probes for turbine test-rig experiments. Recent approaches towards fast-response probes include a waveguide approach by Fioravanti *et al* [14] or studies on the probe head shapes by Liu and Paniagua [15]. Additionally, in consequence of a probe miniaturization, influences on the settling time in turbomachines are discussed by Grimshaw and Taylor [16]. Börner *et al* investigated probes in the wake of transonic turbine cascades [17] and additive manufactured wedge probes in turbine wakes [18]. State-of-the-art measurements of highly unsteady pressure flow fields are commonly acquired with electrical transducers. However, electrical transducers show disadvantages regarding cross-sensitivities against electro-magnetic distortion and the need for active power supply of the electrical components. Electrical sensors can be divided into resistive, piezo-resistive, capacitive and piezo-electric sensors, depending on the measuring principle. In order to exceed limitations of conventional electrical pressure transducers, optical sensors can be used. Previous developments resulted in durable pure glass fiber-optic sensors for surface pressure measurements (see Schmid *et al* [19, 20]). Those fiber-optical pressure sensors use the optical principles of the Fabry-Pérot interferometer.

In a cooperation project between the Chair of Aerodynamics and Fluid Mechanics of the Technical University of Munich, the probe manufacturer Vectoflow GmbH and the fiber-optic sensor specialist fos4X GmbH, an unsteady multi-hole pressure probe equipped with fiber-optic pressure sensors is being investigated. In this paper, the usage of additive manufacturing in the field of aerodynamic pressure probes is described. Furthermore, the development of a fiber-optic pressure sensor based on the Fabry-Pérot interferometer effect is outlined. The aim is to demonstrate the usage of new cylindrical fiber-optic pressure sensors, which are operated differentially. The development steps and the theoretical fundamentals of fiber-optic pressure sensors are given. Moreover, the calibration process for both the spatial and temporal characteristic of the pressure probe is described in detail. In the last part of the paper, experimental investigations which show the characteristics and potential improvements of the sensor over piezo-resistive ones are conducted. A first comparison between piezo-resistive and fiber-optic based pressure sensors is given. In addition, a conventional probe with state-of-the-art piezo-resistive sensors is characterized.

2. Multi-hole probe geometry and additive manufacturing

In the following, the main steps regarding the multi-hole probe geometry and the usage of an additive manufacturing process are presented. The working principle of multi-hole pressure probes relies on the stagnation of the flow around the probe, when being inserted in the flow of any fluid. The pressure distribution around the bluff probe body varies from the maximum pressure at the location of stagnation to lower values, that can even be lower that the static pressure in the undisturbed flow far upstream of the bluff probe body. At the stagnation point maximum pressure, the stagnation or total pressure p_t, is equal to the sum of the static pressure p_s and the dynamic pressure far away from the probe q.
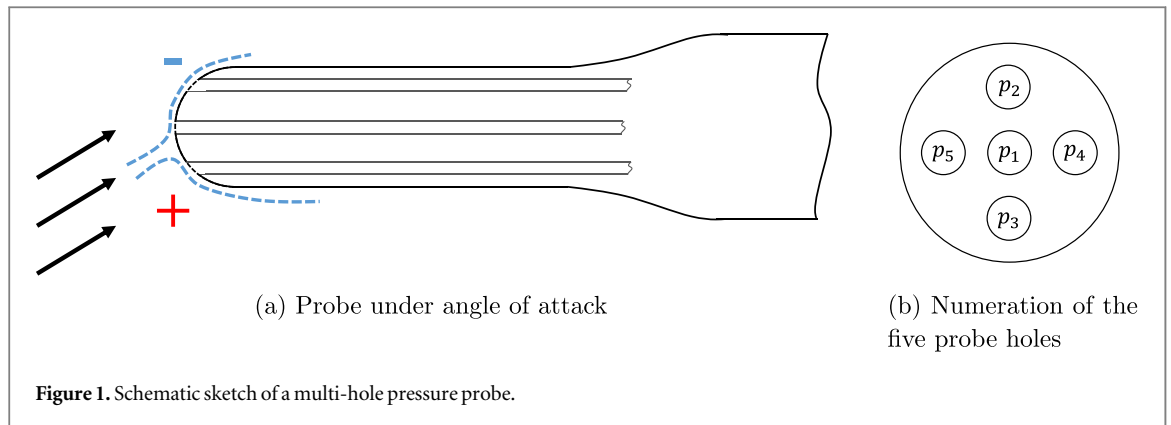
(a) Probe under angle of attack

(b) Numeration of the five probe holes

Figure 1. Schematic sketch of a multi-hole pressure probe.

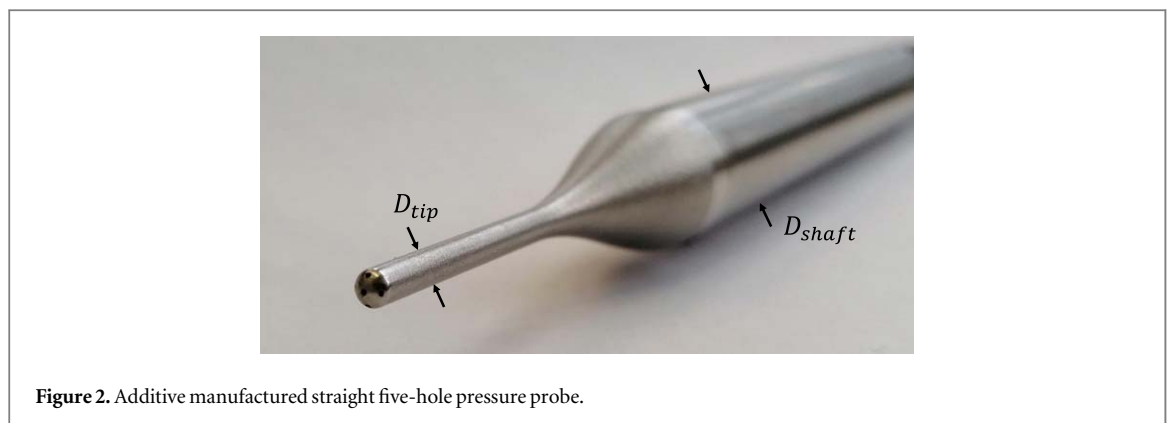**Figure 2.** Additive manufactured straight five-hole pressure probe.

$$p_t = p_s + q = p_s + \frac{\rho}{2} U_\infty^2 \tag{1}$$

Here, U_∞ is the free-stream velocity and ρ the density of the fluid. Similar to the well-known Pitot probe, where the stagnation pressure is measured at a single pressure port, multi-hole probes measure the total pressure of the flow at various locations at the probe tip. In figure 1(a) the schematic cross-section of a multi-hole probe under an angle-of-attack is depicted. In this flow situation the bottom and central hole would experience higher pressures than the upper hole. By measuring all pressures and setting these pressures into relation, the general flow properties at the location of the probe tip can be concluded. For a five-hole probe, which can measure both, pitch and yaw, angles, the pressures $p_1, p_2, ..., p_5$ are measured at the depicted pressure ports (see figure 1(b)). In the present research project, a multi-hole pressure probe is developed for its use in unsteady flows (see figure 2). It is designed for measurements in turbomachinery and wind tunnels. In contrast to steady pressure acquisitions, long pressure lines cannot be used to connect the probe holes to the acquisition manometers/pressure sensors for unsteady flows as the time-dependent pressure fluctuations would be attenuated entirely. Therefore, differential pressure sensors are installed in close proximity to the probe tip—often in the probe shaft. Turbomachinery use cases with signal frequencies of up to 10 kHz define the temporal characteristics. Intrusive effects, as they occur when placing probes in flows, can be avoided by miniaturizing the fast-response pressure probe (FRAP) and its shaft. Using additive manufacturing enables the realization of arbitrary probe shapes, which counteract the limitations of probes manufactured in conventional cutting processes [21].

Fabrication of complex geometries can be realized with additive manufacturing. For the manufacturing of the probe shown in figure 2, the *powder-bed fusion method*, more precisely the *selective laser melting (SLM)* method, was used. Thereby, metal or ceramic powders are melted and sintered. Further terminologies for SLM in the literature are *direct metal laser sintering* or *laser cusing* [21]. In the SLM process, thin layers of powder are stacked on top of each other and selectively melted by a laser. Considering the design of aerodynamic probes, the narrow internal channels and the required tightness make certain manufacturing settings necessary. Layer thicknesses under 50 μm and focal laser diameters of around 100 μm provide good results with relatively small probe diameters. The orientation of the probe during the additive manufacturing process is crucial to obtain a smooth surface, as well. Low angles and overhangs must be avoided when possible. Depending on the potentially harsh environments during probe applications, e.g. high temperatures, different materials can be used in the printing process. The materials, which can be used in the powder-bed-fusion process, have to show adequate melting and resolidifying properties [21]. Materials like titanium, Inconel 718, or stainless steel are most commonly used for aerodynamic applications [22]. In this work's case, it was decided to use the standard alloy

Figure 3. L-shaped probe head comparison: probe after additive manufacturing (left) and after post manufacturing process (right).
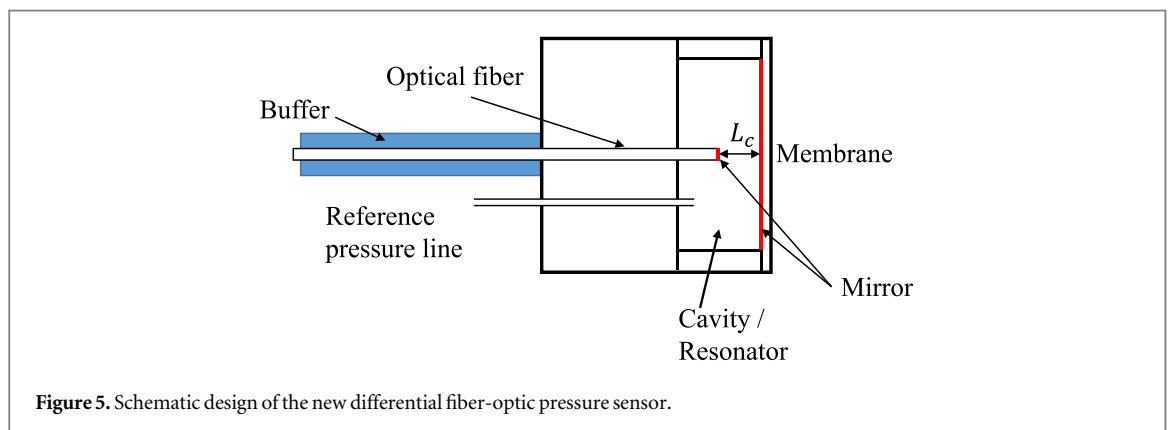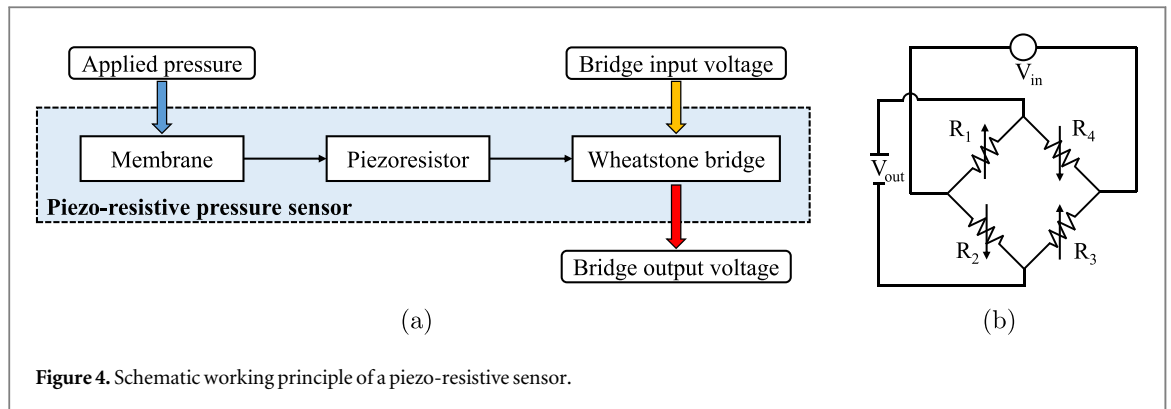
316L, since no special temperature requirements were present. Nevertheless, there are still some limitations regarding the probe's geometry and its channel configuration when setting up the additive manufactoring process. Hence, many iterations are required to achieve acceptable results. These limitations range from powder accumulation within cavities to excessive porosity or rough surfaces in some structures. Research efforts targeting those problems have enabled the manufacturing of arbitrary multi-hole probes with tip diameters of 1.2 mm and channel diameters of $D \ll 1$ mm [22]. As the final step of the manufacturing, different details in the probe design can be realized in a post manufacturing cutting process (see figure 3). Such details can be, for example, different probe tip shapes, which can vary from the application of the probe, or the connection to a probe holder. Most commonly only the probe head is manufactured through SLM, since it is the critical part of the probe and sensible to geometric variations. For most unsteady applications, a hemispheric probe tip is beneficial. Probe geometries can be adopted to special measurement instrumentations. Börner *et al* realized a 3D-printed miniaturized wedge probe for transonic wake flows [18]. Furthermore, Bach *et al* designed a SLM-manufactured guide vane with an integrated Kiel probe [23]. Improvements in the 3D-printing process can lead to further miniaturized probes, which reduce intrusive effects of the probe in the flow field.

3. Sensor specifications

As already mentioned, due to the measurement task in highly unsteady flows, the placement of pressure sensors inside the probe is necessary, since long pressure lines to manometers would attenuate signal contents of high frequencies entirely. In the following, the state-of-the-art pressure sensor type, namely piezo-resistive sensors, are introduced. Furthermore, the development of a new fiber-optic pressure sensor, that should overcome the downsides of the electric counterparts, is described.

3.1. Piezo-resistive sensor
In figure 4(a) the working principle of a piezo-resistive sensor is depicted [24]. Due to the application of pressure, the sensor membrane will be deformed. Therefore, the piezoresistor will experience bending stresses and, hence, changes in electrical resistivity of the sensor material due to the piezo-resistive effect. A Wheatstone bride is embedded in the piezoresistor membrane (often silicon). The change in resistance of the bridge leads to a change in the output voltage V_{out} (see figure 4(b)). Even though piezo-resistive sensors are easy to use and the state-of-the-art solution for pressure measurements, there are several downsides, which lead to the idea to develop a sensor based on another measurement technique, as described in the following chapter. Piezo-resistive sensors show not negligible cross-sensitivities to external influences, like temperature and humidity changes or electro-magnetic disturbance. Furthermore, the Wheatstone bridge has to be operated actively. In addition, due the spatial restrictions inside a pressure probe, the wiring of the multiple sensors is time-consuming and complex. Commercially available differential sensors are seldom smaller than 2–3 mm in diameter, considering the desired pressure range of up to 2 *psig* for low-speed wind tunnel use-cases.

Figure 4. Schematic working principle of a piezo-resistive sensor.

Figure 5. Schematic design of the new differential fiber-optic pressure sensor.

3.2. Fiber-optic pressure sensor

A major part of the probe improvement activities is the enhancement of the sensor performance. Therefore, optical principles are applied to surpass the limits of conventional electrical pressure transducers with respect to resolution and cross-sensitivities. The characteristics of the optical sensors are expected to outperform state-of-the-art piezo-resistive sensors.

In previous developments, fos4X GmbH has developed a durable pure glass absolute fiber-optic pressure sensor for surface pressure measurements [19, 20]. The cuboid pressure sensor, which is wall mounted, operates without any conductive material. Due to its absence, the sensor is inherently immune to electro-magnetic interference. Furthermore, it is robust against water, humidity, and corrosion. The miniature sensor with dimensions of 1.6 mm × 3 mm × 10 mm is capable of measuring aerostatic, aerodynamic and aeroacoustic events as a pressure sensor and as a microphone at the same time [19]. The flat design allows for integration in surfaces with minimal aerodynamic disturbance of the air flow. The fully exposed membrane of 1.65 mm diameter at the surface of the sensor enables pressure measurements without any spectral characterization, because of constant frequency response to 80% of the natural frequency of 250 kHz [19, 20].

In contrast to the existing cuboid absolute pressure sensor, a new cylindrical, differential pressure sensor is developed and tested, in this work. It is intended to be installed in five-hole probes as a replacement for state-of-the-art piezo-resistive sensors.

3.2.1. Fabry-pérot effect for pressure sensing

A fiber-optic pressure transducer at the end of a common telecommunication fiber works in principle similar to their electrical counterparts: The fiber-optic sensor is a passive MOEMS glass chip, which consists of a diaphragm/membrane, a resonance cavity and two mirrors. One mirror is attached on the diaphragm, while the second is half transparent and fixed. Applied pressure p bends the diaphragm and changes the cavity length L_c between the two mirrors (see figure 5). The end of the fiber and the inner part of the membrane represent the two mirrors. The maximum deflection of the membrane is [20]:

$$\Delta L = \frac{3r_m^4(1 - \nu^2)}{16Eh_m^3}p \qquad (2)$$

Here, E is the Young's modulus, ν the Poisson's ratio and r_m and h_m radius and thickness of membrane. Thus, the performance of the measurement system, e.g. its sensitivity, is predominantly defined by the mechanical
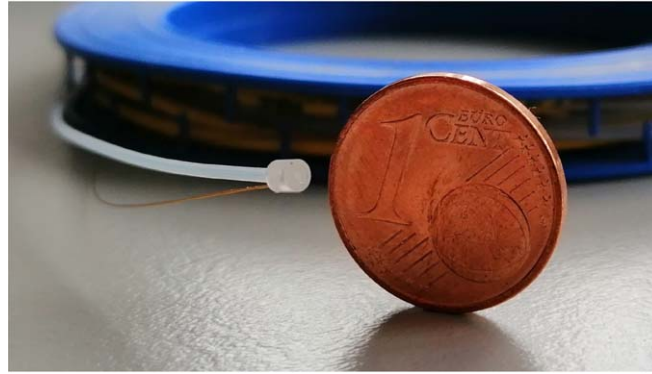
Figure 6. Qualitative size comparison of a sensor prototype and a Euro cent coin.

displacement of the membrane. The miniaturization of the sensor design will therefore considerably affect the sensitivity. A broadband infrared light source illuminates the transducer from the fiber-optic cable. Optical interference modulates the reflecting light spectrum depending on the cavity length and therefore, the deflection of the membrane due to the applied pressure. Each wavelength λ of incoming light, which fulfills the Fabry-Pérot resonance condition will interfere destructively [25]. The ratio of the reflecting light spectrum I_R to the incoming light spectrum I_0 is dependent on the phase δ and can be calculated as follows:

$$\frac{I_R}{I_0} = \frac{M + F \sin(\delta/2)^2}{1 + F \sin(\delta/2)^2} \tag{3}$$

$$\frac{\delta}{2} = \frac{2\pi}{\lambda} n(L_c + \Delta L) \tag{4}$$

Here, F depicts the coefficient of finesse, which describes the quality of the Fabry-Pérot filter. M refers to the 'mismatch' of the reflectance values in the interferometer [26, 27]. An increasing cavity length shifts the phase condition of the destructively interfered wavelength in the spectrum to larger wavelengths, while a smaller cavity length shifts the spectrum to smaller wavelengths [19, 28]. The modulated light is guided back in the same single fiber to the optical measurement device, where it is split in two parts. While the first part is focused directly on a photodiode, the second part is optically filtered and focused on a second photodiode. The reflected spectrum of the sensor is matched to the operating point of an edge-filter interrogator, also known as the Q-point of the device. Therefore, the edge-filter interrogator is filtering a single destructive interference in the optical spectrum in the C-band. The ratio of the light intensities reveals the phase shift of the reflected spectrum. The correlation of this ratio to the applied pressure can be determined in a calibration. The optical filtering process ensures sampling frequencies up to $f_s = 50$ kHz. Each analog signal is converted to a digital value by an analog to digital converter.

3.2.2. Sensor design and assembly

In the development process conducted within this work, a gauge/differential fiber-optic pressure sensor, which is based on the optical principles of a Fabry-Pérot interferometer, is manufactured. As an aim the main specifications of the presented five-hole FRAP shall be improved regarding its measurement abilities by replacing the piezo-resistive sensors with the fiber-optic ones. The fiber-optic sensor casing and membrane are fabricated out of two fused silica (SiO_2) wafers, which are bonded together. Further information regarding the selective laser etching (SLE) bonding process is given in [29]. Furthermore, the optical fiber is fixed to fit the Q-Point of the measurement device in the micromachined wafer. A capillary is bonded to either pressurize the cavity and therefore measure the differential pressure or work as a gauge sensor with the surrounding static pressure as the reference pressure (see figure 5). In figure 6, a fiber-optic pressure sensor of the 1st generation is shown, which has a diameter of 2 mm. The light is reflected by a mirror and terminated.

4. Probe calibration process

Using the probe in an experiment with unknown flow conditions requires a calibration of the probe beforehand. In the calibration process, a separation of spatial and temporal behavior of the probe is assumed. Hence, besides an aerodynamic/spatial calibration, a dynamic/temporal calibration has to be conducted as well. The temporal calibration characterizes the acoustic system in the channels between the tip and the sensors. Both calibration approaches are explained in more detail in the following sections.

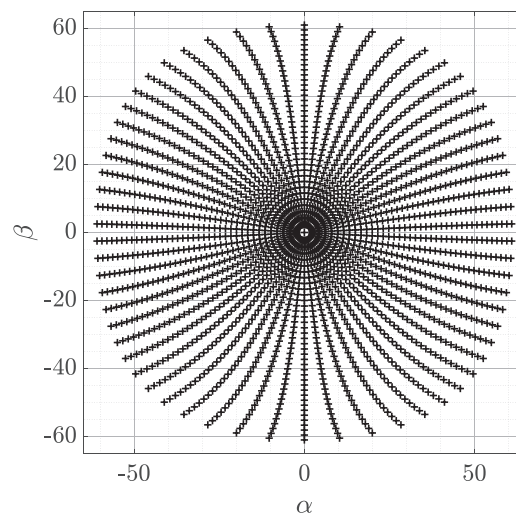**Figure 7.** Free-jet calibration facility at Vectoflow [22].

Figure 8. Calibration grid for $\alpha, \beta = \pm 60°$.

Table 1. Specifications of the Vectoflow calibration wind tunnel [22].

Velocity range	$Ma \leqslant 1.2$
Maximum power	90 kW
Angle range	$\pm 165°$ (yaw), $\pm 180°$ (roll)
Temporal speed non-uniformity	$\pm 0.25\%$ at $Ma = 0.1$
Nozzle diameter	30–200 mm

4.1. Spatial calibration in a free-jet

Within the spatial calibration, the correlation between the mean free-stream flow conditions and the measured pressures at the probe is determined. Therefore, various combinations of the free-stream velocity U_∞ and the flow angles α and β are set in the free-jet calibration wind tunnel, which is illustrated in figure 7.

Table 1 depicts the specifications of the calibration free-jet facility. Depending on the expected angle and velocity range in later experiments, angle combinations at certain velocities are calibrated. Figure 8 shows the calibration grid for the straight five-hole probe in figure 2. Figure 9 shows the two interchangeable coordinate systems: pitch(α)-yaw(β) or roll(ϕ)-cone(θ).

$$\alpha = \tan^{-1}(\tan(\theta)\sin(\phi)) \tag{5}$$

$$\beta = \sin^{-1}(\sin(\theta)\cos(\phi)) \tag{6}$$

$$\theta = \cos^{-1}(\cos(\alpha)\cos(\beta)) \tag{7}$$
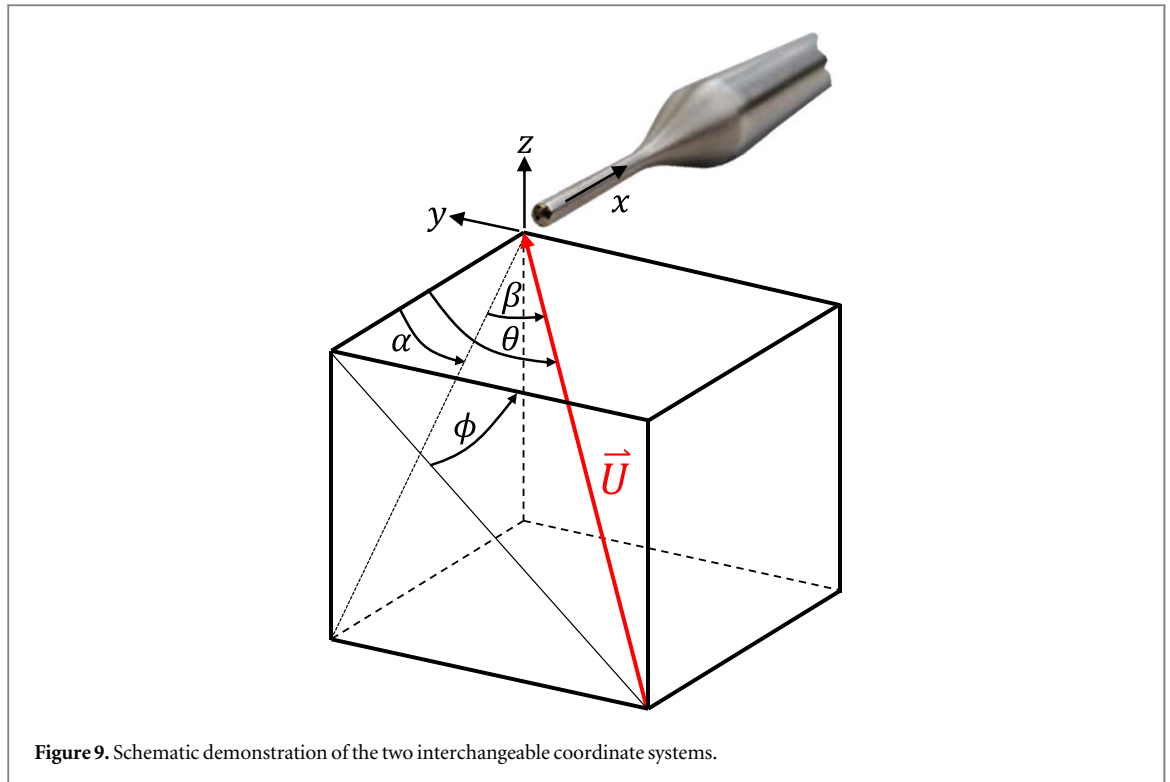
Figure 9. Schematic demonstration of the two interchangeable coordinate systems.
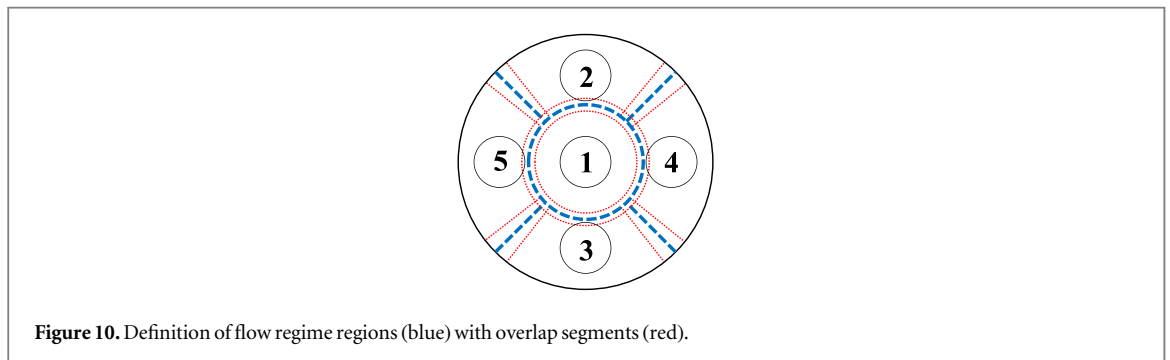

Figure 10. Definition of flow regime regions (blue) with overlap segments (red).

$$\phi = \tan^{-1}(\sin(\alpha)/\tan(\beta)) \qquad (8)$$

In order to determine the actual flow conditions at the probe tip in an experiment, the acquired pressures have to be post-processed. In the literature, there are multiple ways how the calibration data is used for reconstructing the flow-field properties. The most commonly used one is an interpolation scheme, which is applied on the gathered pressures in order to calculate the properties at the probe tip. System identification approaches with the use of neural networks can also be found in the literature. Both approaches will be discussed and compared subsequently:

Non-dimensional calibration coefficients can be calculated, which are the basis for the interpolation. The interpolation routines can be divided in global or local interpolations, depending on whether to use all calibration points or solely points in the surrounding with similar calibration coefficient values, respectively. Based on Johansen [30], a local interpolation method is used and the calibration data is divided in a low-angle and high-angle regime. The pressure port with the highest measured pressure determines the set of calibration coefficients, that are used for the reconstruction. In the case that multiple pressure ports see similar pressures within a pre-specified margin, overlap segments are defined, in which the coefficients are calculated for every dominant pressure port (see figure 10). For the low-angle regime, where the central port p_1 measures the highest pressure, the coefficients are as follows:

$$b_\alpha = \frac{p_3 - p_2}{\bar{q}} \qquad b_\beta = \frac{p_4 - p_5}{\bar{q}} \qquad (9)$$

$$A_t = \frac{p_1 - p_t}{\bar{q}} \qquad A_s = \frac{p_t - p_s}{\bar{q}} \qquad (10)$$
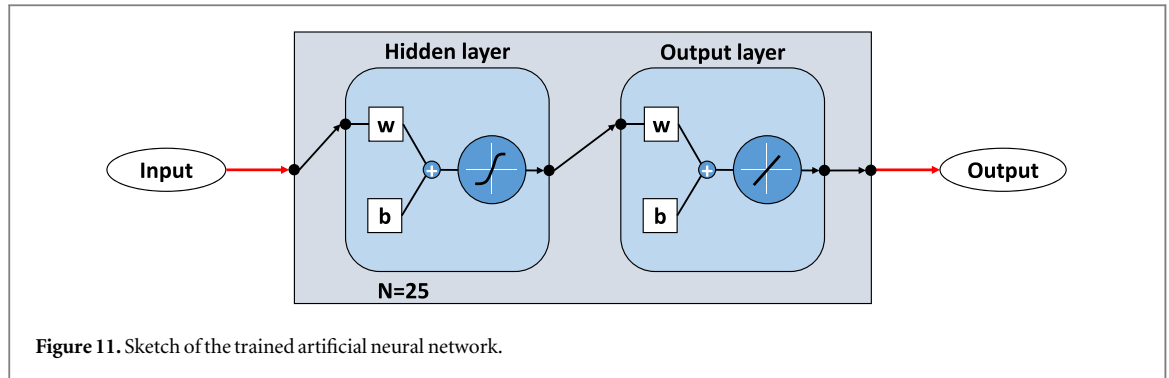
Figure 11. Sketch of the trained artificial neural network.

$$\text{with} \quad \bar{q} = p_1 - \frac{p_2 + p_3 + p_4 + p_5}{4} \tag{11}$$

Thus, $\bar{q}$ denotes the pseudo dynamic pressure, which is used to non-dimensionalize the coefficients.

The high-angle regime, where one of the circumferential ports p_i measures the highest pressure, can be described by the following coefficients:

$$b_\theta = \frac{p_i - p_1}{\bar{q}} \qquad b_\phi = \frac{p^+ - p^-}{\bar{q}} \tag{12}$$

$$A_t = \frac{p_i - p_t}{\bar{q}} \qquad A_s = \frac{p_i - p_s}{\bar{q}} \tag{13}$$

$$\text{with} \quad \bar{q} = p_i - \frac{p^+ + p^-}{2} \tag{14}$$

Thereby, p^+ and p^- denote the pressures at the circumferential pressure ports in clockwise and counter-clockwise direction.

In the reconstruction procedure, the pressure data at the test point is acquired $p_{1,T}$, $p_{2,T}$, ..., $p_{5,T}$. The subscript T denominates the values at the test point T. The non-dimensional coefficients $b_{\alpha,T}$, $b_{\beta,T}$ or $b_{\theta,T}$, $b_{\phi,T}$ for low- or high-angle regimes are calculated as defined above, respectively. In the following step, a local-least square interpolation determines the quantities $A_{t,T}, A_{s,\,T}$ and α_T, β_T or θ_T, ϕ_T as functions of $f\,(b_{\alpha,T},\,b_{\beta,T})$ or $f\,(b_{\theta,T},\,b_{\phi,T})$. The Mach number Ma can be calculated as follows (shown for the high-angle regime):

$$p_t = p_i - A_{t,T} \cdot \bar{q}_T \tag{15}$$

$$p_s = p_i - A_{s,T} \cdot \bar{q}_T \tag{16}$$

$$Ma = \sqrt{\frac{2}{\kappa - 1} \cdot \left(\left(\frac{p_t}{p_s} \right)^{\frac{\kappa - 1}{\kappa}} - 1 \right)} \tag{17}$$

$$U = Ma \cdot c = Ma \cdot \sqrt{\kappa \cdot R \cdot T} \tag{18}$$

Here, c is the speed of sound, κ the specific heat ratio and R the specific gas constant. Lastly, the velocity components u, v and w can be calculated:

$$u = U \cdot \cos(\alpha) \cdot \cos(\beta) \tag{19}$$

$$v = U \cdot \sin(\beta) \tag{20}$$

$$w = U \cdot \sin(\alpha) \cdot \cos(\beta) \tag{21}$$

A possible way to implement the basic interpolation functionality in MATLAB is to use the built-in Delauney triangulation function *delauneyTriangulation* from a set of points. Using its object function *pointLocation*, the triangle enclosing a test point and the barycentric coordinates of the test point can be determined. Thus, a fast interpolation can be ensured.

A further method how the measured pressures can be post-processed is the usage of system identification methods. Neural network approaches have been used in the field of multi-hole probes for the reconstruction of the flow conditions [31, 32]. An artificial neural network (ANN) application is based on training data to set the weights of connected neurons/nodes. So-called weights and biases determine the strength of the connections between different neurons and layers. MATLAB offers the neural network fitting application *nftool* [33]. Figure 11 shows the structure of the trained neural network for a single calibration Mach number. As input data, the five measured pressures are given. The output of the ANN are the flow angles (α and β) and the static and total pressure (p_s and p_t). The neural network is trained with the function *trainlm*, which trains a shallow two layer feed-forward network with sigmoid hidden neurons and linear neurons. For this purpose, the
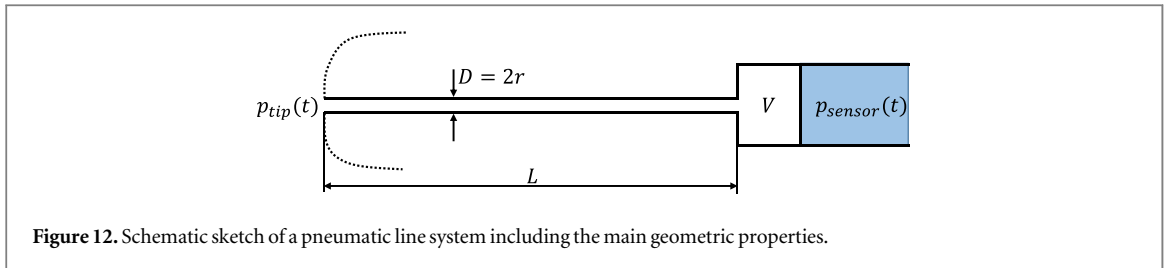
Figure 12. Schematic sketch of a pneumatic line system including the main geometric properties.

Levenberg-Marquardt backpropagation algorithm is applied to update the weight *w* and bias *b* values [34]. The division between training, validation and test data for the neural network fitting is random. The number of hidden neurons is set to $N = 25$.

4.2. Temporal calibration

In addition to the spatial calibration, the dynamic characteristics of the multi-hole probe has to be determined. The acoustic system inside the pressure channels has a significant influence on the measurement of unsteady flow phenomena. Figure 12 illustrates the properties, which mainly describe the acoustic system between the tip and the location of the sensor inside the probe shaft: the length L, the diameter $D = 2r$ and the volume in front of the sensor V. The acoustic system is mainly dominated by two different forms of pressure distortion, resonance and attenuation.

A way to describe the dynamic behavior of pneumatic line-cavity systems was introduced by Bergh and Tijdeman [35]. They analytically formulated a recursive solution for small disturbances and for tubes with small diameters compared to the tube length $L/D \gg 1$. Furthermore, a laminar flow and a fluid governed by the ideal gas law was assumed. The complex ratio P_{sensor}/P_{tip} describes the attenuation and phase shift for the acoustic wave propagation inside a system of a single tube and is denoted as transfer function (TF) of the system $H(\omega)$:

$$H(\omega) = \frac{P_{sensor}(\omega)}{P_{tip}(\omega)} = \left[\cosh(\psi L) + \frac{V\eta\psi}{\kappa\pi r^2} \sinh(\psi L) \right]^{-1} \tag{22}$$

$$with \qquad \psi = \frac{\omega}{c}\sqrt{\frac{\kappa}{\eta}\frac{J_0(\gamma)}{J_2(\gamma)}} \tag{23}$$

$$\eta = \left[1 + \frac{\kappa - 1}{\kappa}\left(\frac{J_2(\gamma\sqrt{Pr})}{J_0(\gamma\sqrt{Pr})} \right) \right]^{-1} \tag{24}$$

$$\gamma = i^{3/2}r\sqrt{\frac{\rho\omega}{\mu}} \tag{25}$$

Thereby, J_i denotes the Bessel function of ith order, κ the specific heat ratio and Pr, ρ and μ the Prandtl number, the density and dynamic viscosity of the fluid, respectively.

In the case of longer pneumatic lines, the signal noise can get dominant in the deconvolution. Semaan and Scholz compare the Bergh and Tijdeman correction with a method using a Wiener filter. This approach is called Wiener deconvolution [36]. They come to the conclusion that only for a length bigger than $L > 150$ mm the Wiener deconvolution is beneficial. Since the probe presented in this paper has shorter tubes, the Bergh and Tijdeman solution is used as a reference in the following.

Experiments with additive manufactured probes have shown that due to imperfections inside the tubing, analytic solutions can solely serve as a first guess. The need for more accurate transfer functions leads to the experimental verification of the acoustic system. In a frequency test-rig the investigated object (e.g. the multi-hole probe) and a reference sensor are mounted in close proximity to each other (see figure 13). Furthermore, it contains a speaker connected to an amplifier. Sinusoidal waves are emitted and recorded at specified frequency steps, and hence, the amplitude ratio as well as the phase shift are obtained.

When measuring in unknown unsteady flows, the reconstruction process of the actual time signal at the tip is shown in figure 14 [10]. The quasi-periodic signal at the sensor $p_{sensor}(t)$ represents the input. Before the time-domain signal is processed into the frequency domain by applying a fast Fourier transformation (FFT), a windowing function is applied. The TF is then used to calculate the Fourier-transformed pressure at the tip $P_{tip}(\omega)$ from the Fourier-transformed pressure at the sensor $P_{sensor}(\omega)$:

$$P_{sensor}(\omega) = H(\omega)P_{tip}(\omega) \tag{26}$$

Furthermore, digital signal conditioning, like low-pass filtering, can be applied in this step. Lastly, the signal is transferred into time space by applying the inverse FFT. The pressure at the tip $p_{tip}(t)$ is obtained as the output and can be further processed by utilizing the spatial calibration data. In order to show the functionality of the
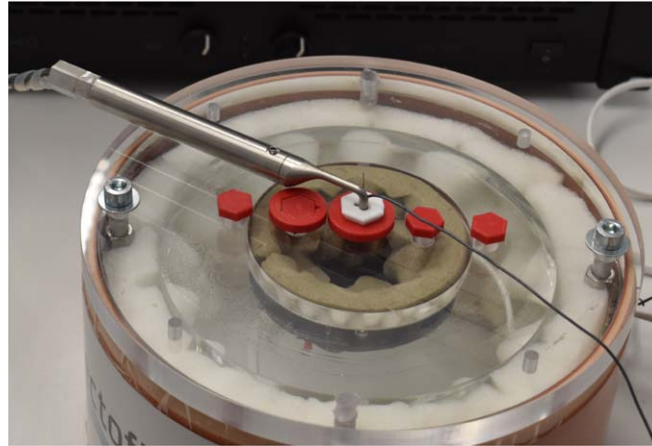
Figure 13. Frequency test-rig for the experimental determination of the acoustic transfer function $H(\omega)$.
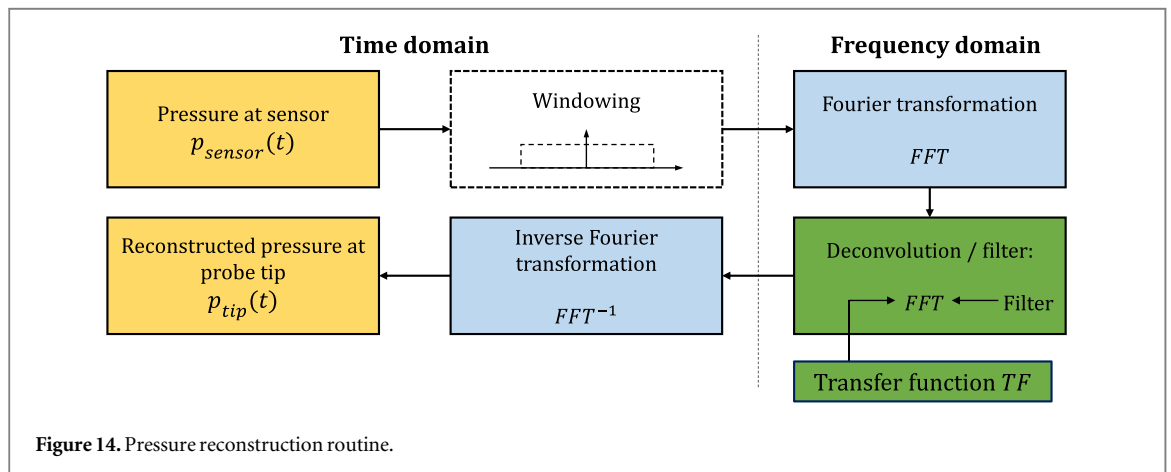

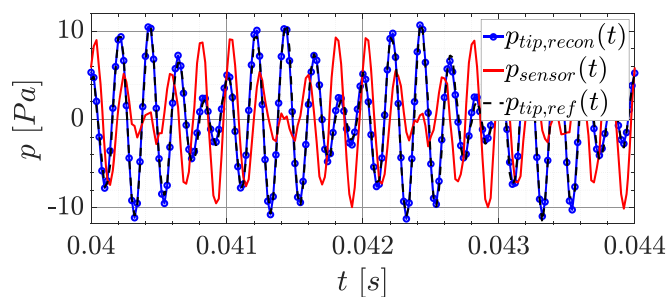**Figure 14.** Pressure reconstruction routine.

Figure 15. Pressure reconstruction in a narrow tubing: Superposition of sinusoidal signals with $f_1 = 4000$ Hz and $f_2 = 5000$ Hz.

reconstruction procedure, the transfer function of a narrow silicone tubing is determined. Two sinusoidal signals with $f_1 = 4000$ Hz and $f_2 = 5000$ Hz with differing weights are superposed and emitted by the speaker in the frequency test-rig. Figure 15 shows the reconstructed pressure at the tubing tip $p_{tip,recon}$ after applying the TF on the pressure detected at the sensor p_{sensor}. It is compared to a reference signal measured in close proximity to the tip with another sensor $p_{tip,ref}$. The reconstructed signal matches the reference signal very well.
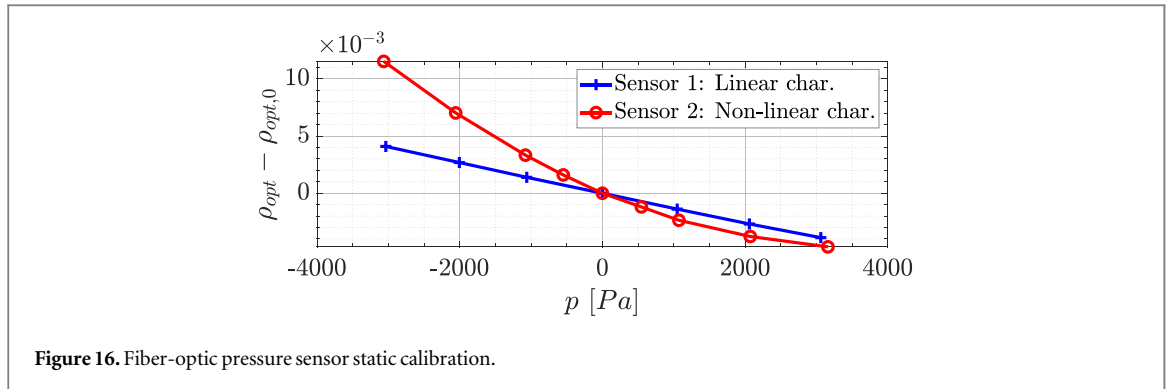
Figure 16. Fiber-optic pressure sensor static calibration.

5. Sensor and probe characterization

5.1. Sensor tests

In the following, all experiments are conducted with ten sensors of the first sensor generation (depicted in figure 6). Tests include the determination of the calibration coefficient and comparisons to piezo-resistive sensors.

5.1.1. Static and dynamic calibration

In the sensor calibration process, the correlation between the optic output value ρ_{opt} and the applied pressure p is determined for the linear pressure range by

$$\rho_{opt} = k \cdot p + \rho_{opt,0}.$$

(27)

If the operating point is set correctly, the characteristic should be linear, since it is mainly dependent on the mechanic deformation of the sensor membrane. In addition, the operating point has been set to match the quasi-linear range of the edge-filter. By applying predefined pressures, either statically or dynamically, the calibration coefficient k is calculated. First calibration tests have shown that the sensor's behavior strongly depends on the ambient conditions and the installation situation. Therefore, it is important to know the influence of these conditions during calibration and to separate them in the best possible way. Temperature resistance is limited due to the use of adhesive when attaching the optical fiber and the pressure capillary to the ferrule. In addition, the temperature sensitivities vary from sensor to sensor, but behave linearly. For the static calibration procedure, a sealed box, in which the sensor was integrated, was pressurized. The sensors' output values are linear with pressure in a pressure range specific for each sensor. The width of this range depends mostly on the sensitivity of the sensor and the Q-point. Outside of the range, non-linear behavior sets in. Figure 16 shows the static calibration curves for two sensors. One of the sensors shows a linear correlation between pressure and the optical output value $\rho_{opt} - \rho_{opt,0}$ over the whole shown pressure range. The linear range of the other sensor is less extensive, so that an overall non-linear behavior in the shown measurement range was observed. For future sensor generations, the sensor assembly and setting of the operating point is one of the most challenging tasks in order to have reproducible linear behavior ranges for sensors in the same batch. Nevertheless, even for sensors with non-linear static calibration behavior, small, dynamic disturbances around the operating point can be regarded linear. The sensors are tested on their dynamic behavior with a sound generator that produces a specific sinusoidal signal at a prescribed sound pressure level L_p.

5.1.2. Comparison to piezo-resistive sensors

As a first comparison of the fiber-optic pressure sensors to state-of-the-art piezo-resistive sensors, both sensors are placed next to each other in the frequency test-rig. Sinusoidal excitations in the frequency range of $f_s = [100, 1000]$ Hz are measured and compared. The signal frequencies can be exactly reproduced by both sensor types with relative errors smaller than 1% in the whole frequency range. Figure 17 shows the dynamic pressure amplitudes measured by both sensors. Furthermore, the relative deviation of the fiber-optic pressure sensor to the piezo-resistive sensor is depicted. It can be observed that the amplitudes also match very well. Larger deviations at $f_s = 100, 400$ Hz could be due to acoustic modes in the frequency test-rig, that have been observed in previous measurements, as well. Furthermore, those errors could be traced back to the small excitation magnitudes, which are in the range of the minimum transducer resolution.

    Tests examining the noise level of the measurement chain are conducted. The piezo-resistive sensor is connected to a NI 9237 module and shows better signal-to-noise ratios (SNR) than the fiber-optic pressure sensors. This is due to the lack of enhanced signal conditioning in the optic measurement acquisition. The optic
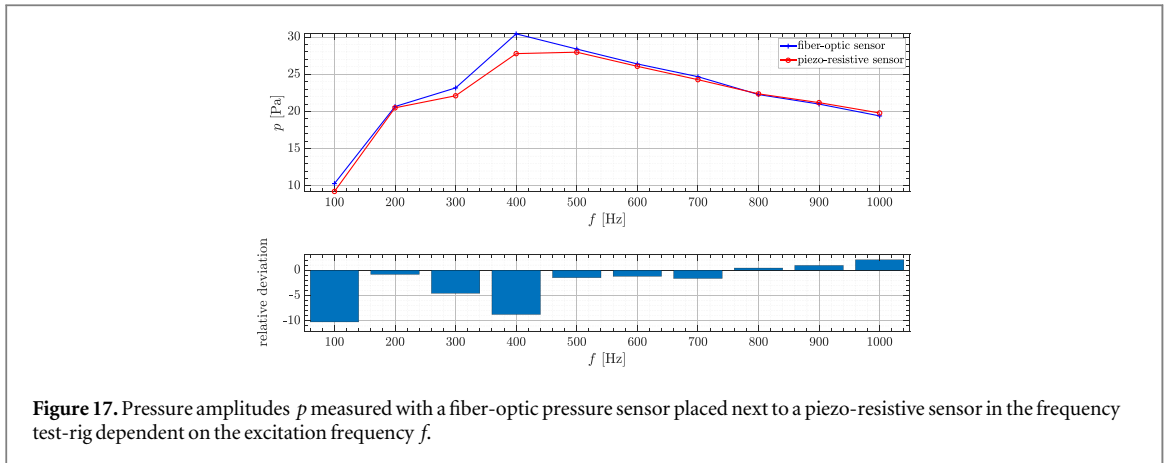
Figure 17. Pressure amplitudes p measured with a fiber-optic pressure sensor placed next to a piezo-resistive sensor in the frequency test-rig dependent on the excitation frequency f.
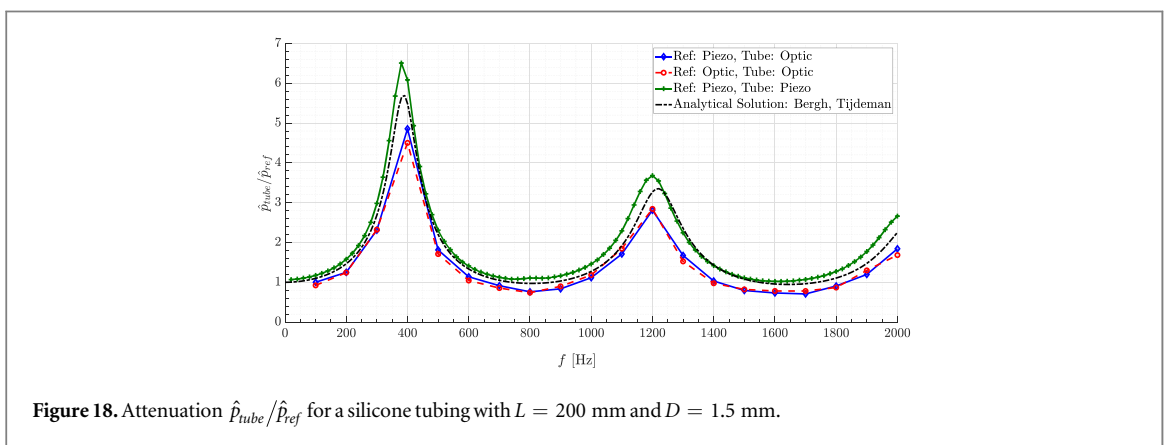

Figure 18. Attenuation $\hat{p}_{tube}/\hat{p}_{ref}$ for a silicone tubing with $L = 200$ mm and $D = 1.5$ mm.

Table 2. Comparison of the fiber-optic pressure sensor specifications to the piezo-resisitve transducer.

		Fiber-optic pressure sensor	Meggitt Endevco 8507C-2
Dimensions (diameter $\times$ depth)	[mm $\times$ mm]	2.0×2.0	2.3×12.7
Pressure range	[kPa]	100	14
Maximum operating temperature	[°C]	120	107
Resonance frequency	[kHz]	290	70

measurement chain is still under development and efforts concerning bandwidth and noise specifications have to be addressed either by changes in hard- or software.

In table 2, a short comparison of the 1st generation fiber-optic pressure sensor specifications, which are observed in the sensor batch, to the Meggitt Endevco 8507C-2 piezo-resistive sensor is shown.

5.1.3. Transfer function of a silicone tubing

A more realistic test application for the fiber-optic pressure sensors is the determination of the transfer function of a silicone tubing with $L = 200$ mm and $D = 1.5$ mm. Experiments are conducted in the aforementioned frequency test-rig. Variations of the combination of the reference sensor and the sensor at the end of the tubing are compared. Different frequency step sizes were used for the different combinations: 20 Hz for piezo-piezo and 100 Hz for the piezo-optic and optic-optic cases, respectively. Moreover, the analytical solution for the attenuation $\hat{p}_{tube}/\hat{p}_{ref}$ by Bergh and Tijdeman is displayed in figure 18. For the two cases, in which the fiber-optic sensor is mounted at the end of the tubing, the resonance frequencies match the ones of the analytical and the piezo-piezo solution, which can be seen as the state-of-the-art and validated solution. The qualitative trend is reproduced well, however, the amplitudes of the attenuation are underpredicted by the optic sensors. A possible reason for this can be a systematic error, which is attributed to a modification of the operating point of the sensor while installing it in the test-rig. The fiber-optic sensor is deformed by the surrounding silicone tubing marginally but sufficient enough to cause a change in the calibration coefficient. This leads to the conclusion that
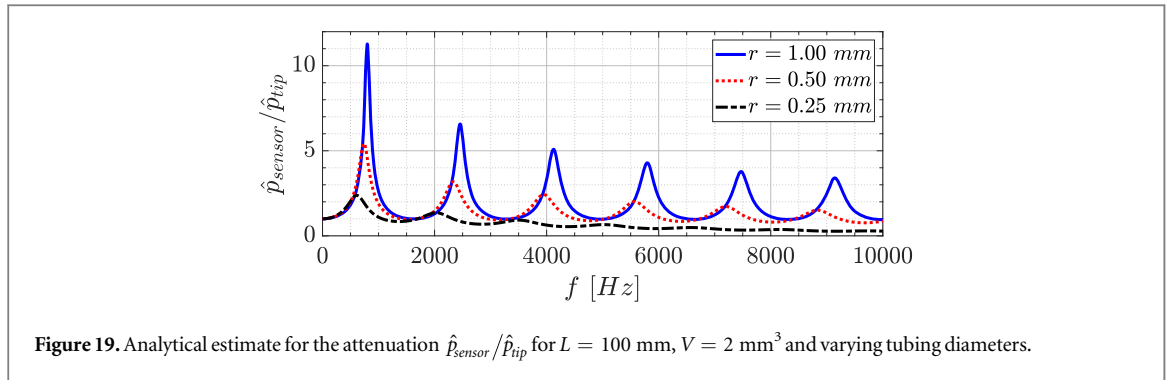
Figure 19. Analytical estimate for the attenuation $\hat{p}_{sensor}/\hat{p}_{tip}$ for $L = 100$ mm, $V = 2$ mm^3 and varying tubing diameters.

Table 3. Five-hole probe and calibration properties.

Probe/tip shape	straight/hemispheric
Tip diameter D_{tip}	3 mm
Shaft diameter D_{shaft}	15 mm
No. channels/holes	5
Channel diameter	$\leqslant 1$ mm
Sensor	Meggitt Endevco 8507C-2
Sensor diameter	2.3 mm
Aerodynamic calibration	$\pm 55°$
Dynamic calibration	10 kHz

the assembly of the sensor into a test object is crucial regarding its behavior and therefore has to be addressed in the future carefully.

5.2. Fast response probe tests

Lastly, the characteristics of a conventional unsteady probe, which is equipped with state-of-the-art piezo-resistive sensors, are shown. For applications with limited space for the probe installation, a miniaturization of the probe dimensions would be beneficial. In addition, a smaller probe head leads to less intrusive and disturbing effects in the flow field. Thus, the reduction of the tip size would enhance the aerodynamic/spatial resolution of the probe [16]. Non-uniform flow conditions, like shear and gradient dominated flows, can be represented in more detail with an increased resolution. Moreover, corrections for flow phenomena due to the intrusion of the probe, like inertial effects of the probe, have a smaller contribution to the pressure measurement. Yet, the reduction of the probe size has also antagonistic effects: Two major problems concerning the temporal characteristic emerge, which affect the acoustic system inside the probe and therefore, predominantly change the unsteady behavior of the pressure probe. First, a reduction of the acoustic channel diameter leads to a high attenuation of the acoustic wave for higher frequencies (see figure 19). Second, sensor dimensions have to be reduced as well when reducing the overall dimensions of the probe and keeping the channel length constant. Flush mounted sensors could counteract the described attenuation. Nevertheless, by placing the sensors in close proximity to the probe tip, the packaging effort and the probe dimensions would increase. Therefore, the performance of future sensors has to be optimized, which is one major driver in the already mentioned development of a new fiber-optic pressure sensor.

5.2.1. Design of a conventional unsteady multi-hole probe

An unsteady five-hole pressure probe, which is displayed in figure 2, has been designed for testing its unsteady aerodynamic measurement behavior. Table 3 summarizes the major design aspects, which are described in more detail in the following. The straight probe has a tip diameter of $D_{tip} = 3$ mm. The additive manufactured probe head is attached to a shaft with an outer diameter of $D_{shaft} = 15$ mm. Five cavities are drilled into the rear part of the probe head, which contain the unsteady differential pressure sensors. For this pressure probe, state-of-the-art piezo-resistive Meggitt Endevco 8507C-2 transducers are installed inside the cavities [37]. A challenging task in the design is the integration of the sensors inside the probe. Considering the miniaturization of the probe, the sensor, which has a diameter of 2.3 mm, limits the geometric design. A further reduction of the size of the probe shaft, which contains five sensors in a compact pattern, is restricted by mechanical stability. In order to avoid leakage, the sensor is surrounded with a thin silicone tubing and pressed into the cavity (see figure 20). The
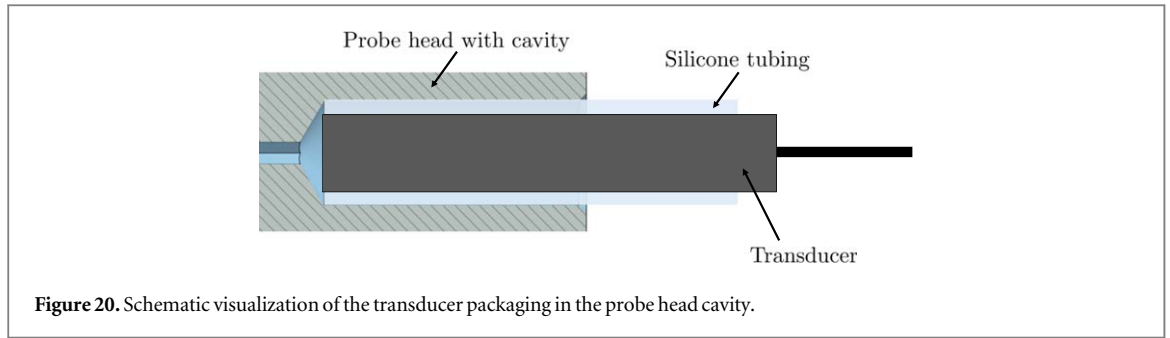
Figure 20. Schematic visualization of the transducer packaging in the probe head cavity.
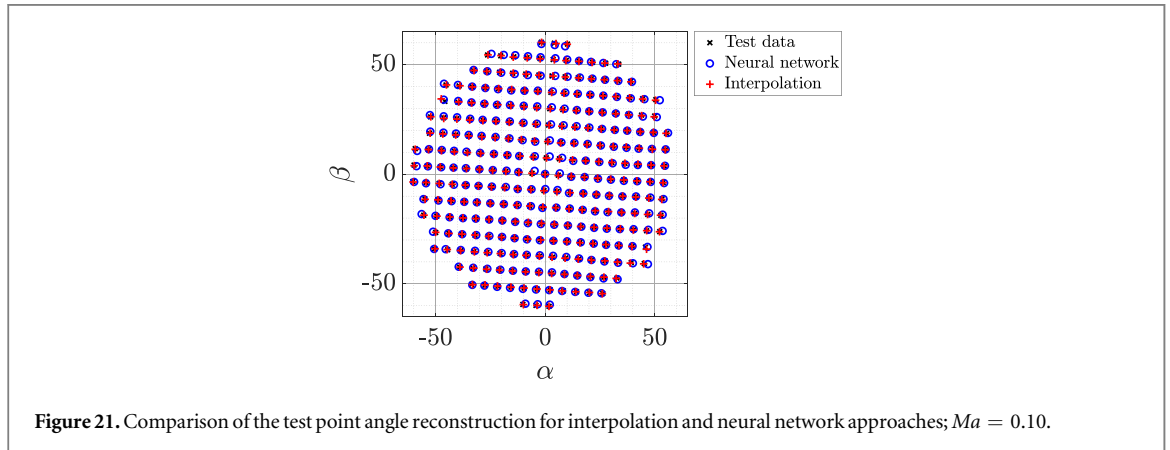

Figure 21. Comparison of the test point angle reconstruction for interpolation and neural network approaches; $Ma = 0.10$.

Table 4. Spatial reconstruction results for both approaches.

| | $\Delta\alpha$ [°] | | | $\Delta\beta$ [°] | | |
	maxabs	*rms*	*std*	*maxabs*	*rms*	*std*
Interpolation	0.74	0.16	0.16	0.76	0.12	0.11
ANN	1.80	0.53	0.50	1.13	0.35	0.35

reference pressure lines of the differential transducer are merged in a manifold, so only one pressure tubing is connected to the reference pressure.

In general, maximum calibrated angles for five-hole probes range up to 60°. Precise reconstructions with absolute angular errors smaller than 1° and velocity errors smaller than 1 m s^{-1} can be ensured up to α, $\beta = \pm 55°$, as it is noted in the subsequent chapter .

5.2.2. Spatial and temporal characteristic

In the following, the post-processing accuracy and time consumption of the two different spatial reconstruction approaches, the local interpolation and neural network, are compared. As a test, data for 258 test points are acquired after the probe calibration for a defined Mach number of $Ma = 0.10$. Figure 21 depicts the post-processed angles compared to the actual angles set in the free-jet wind tunnel. Both methods show mean absolute errors below 1° for both angles. Table 4 shows maximum absolute (maxabs) errors, root-mean-squared (rms) values and standard deviations (std) for both angles. The Delauney triangulated interpolation calculation result in smaller deviations compared to the ANN approach. This is due to a limited amount of neurons in the ANN training of 25 neurons. Nevertheless, both methods show acceptable errors for tested angles up to 60°. The reconstructed velocities match the fixed velocity in the free-jet with relative errors smaller than 1% for both methods. Applying the MATLAB built-in functions for both methods results in a speed-up factor of up to 5 for the neural network processing in comparison to the Delauney triangulated interpolation method. The demand of fast data processing increases, when measuring in highly unsteady flows with sampling frequencies bigger than $f_s > 50$ kHz. Though interpolation methods are optimized and represent the state-of-the-art solution for multi-hole probe post-processing, the neural network approach may lead to reduced calculation times.

As described in the chapter for the probe calibration, besides a spatial calibration, the temporal characteristic has to be determined in the frequency calibration test-rig. For the determination of the transfer function, a
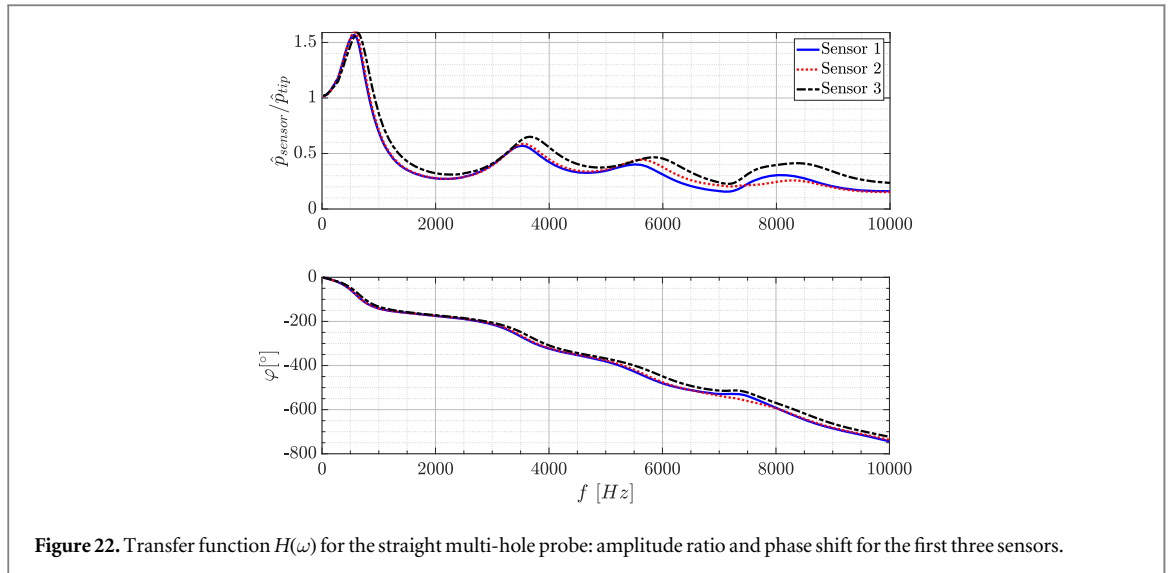
Figure 22. Transfer function $H(\omega)$ for the straight multi-hole probe: amplitude ratio and phase shift for the first three sensors.

frequency step size of the input sinusoidal signal is set to 20 Hz. Figure 22 exemplarily shows the amplitude ratio $\hat{p}_{sensor}/\hat{p}_{tip}$ and the phase shift φ for three of the five sensors of the five-hole FRAP. For frequencies up to 10 kHz, the attenuation does not fall below 0.15. This value is assumed to be appropriate to reconstruct signals within the frequency range. Having calibrated both, the spatial and temporal, characteristics, the fast-response multi-hole pressure probe is ready to be used in unsteady, unknown flow-fields.

6. Discussion and outlook

A reference five-hole pressure probe with piezo-resistive sensors that can measure unsteady phenomena up to 10 kHz was developed, as a preliminary stage towards a fiber-optic based multi-hole probe. Additive manufacturing (selective laser melting) enables the realization of arbitrary probe shapes. Hence, even in probe installation situations with massive spatial restrictions, appropriate probe designs can be achieved and produced. The spatial and temporal calibrations of the five-hole probe ensure a precise reconstruction of the flow-field parameters at the probe tip. The spatial calibration data represents the correlation between the port pressures to the flow conditions that were set during the calibration in the free-jet wind tunnel. When measuring an unknown flow field, the calibration data set can be used to reproduce the unknown conditions, either by interpolation or neural network approaches. During the temporal calibration, the acoustic system inside the probe pressure channels is characterized. A transfer function that determines the amplitude ratio and the phase shift of the pressures in the channels is obtained experimentally in a frequency test-rig. The development of an unsteady fiber-optic pressure sensor is presented. The gauge/differential fiber-optic sensor is based on the optical principles of a Fabry-Pérot interferometer. Details on the optic theory are given. Tests with the fiber-optic pressure sensors of the 1st sensor generation already show good dynamic behavior and appropriate specifications in comparison to state-of-the-art electrical sensors. The static calibration shows the importance of a precise sensor assembly in order to fit the operating point of the sensor to the linear part of the edge-filter interrogator spectrum. In case of discrepancies in the assembly, the sensor output could behave non-linear when larger pressure amplitudes are applied. In future developments, further sensor investigations have to be carried out with respect to fixed mounting and assembly conditions. In addition, improvements concerning signal conditioning within the optical measurement chain will be examined. In future development steps, a smaller unsteady multi-hole probe equipped with the differential fiber-optic pressure sensors will be assembled, calibrated and tested.

Acknowledgments

ORCID iDs

Florian M Heckmeier ⬤ https://orcid.org/0000-0002-1130-729X

References

[1] Ainsworth R W, Miller R J, Moss R W and Thorpe S J 2000 *Meas. Sci. Technol.* **11** 1055–76
[2] Babinsky H, Kuschel U and Hodson H 2000 The aerodynamic design and use of multi-sensor pressure probes for MEMS applications *15th Bi-Annual Symposium on Measuring Techniques in Transonic and Supersonic Flows in Cascades and Turbomachines (Florence, Italy)*
[3] Lengani D, Paradiso B and Marn A 2012 *J. Therm. Sci.* **21** 21–31
[4] Gossweiler C R, Kupferschmied P and Gyarmathy G 1995 *J. Turbomach.* **117** 611
[5] Humm H J, Gossweiler C R and Gyarmathy G 1995 *J. Turbomach.* **117** 618
[6] Kupferschmied P, Köppel P, Roduner C and Gyarmathy G 2000 *J. Turbomach.* **122** 505
[7] Roduner C, Kupferschmied P, Köppel P and Gyarmathy G 2000 *J. Turbomach.* **122** 517
[8] Köppel P, Roduner C, Kupferschmied P and Gyarmathy G 2000 *J. Turbomach.* **122** 527
[9] Rediniotis O, Johansen E, Tsao T, Seifert A and Pack L 1999 MEMS-based probes for velocity and pressure measurements in unsteady and turbulent flowfields *37th Aerospace Sciences Meeting and Exhibit c (Reston, Virigina: American Institute of Aeronautics and Astronautics)*
[10] Rediniotis O, Allen R, Zeiger M and Johansen E 2003 Embedded-Sensor, Fast-Response Multi-Hole Probes *41st Aerospace Sciences Meeting and Exhibit (Reno, Nevada: American Institute of Aeronautics and Astronautics)*
[11] Persico G, Gaetani P and Guardone A 2005 *Meas. Sci. Technol.* **16** 1741
[12] Sieverding C H, Arts T, Dénos R and Brouckaert J F 2000 *Exp. Fluids* **28** 285–321
[13] Brouckaert J F 2007 *Proc. Inst. Mech. Eng. Part A J. Power Energy* **221** 811–3
[14] Fioravanti A, Lenzi G, Ferrara G and Ferrari L 2016 *J. Eng. Gas Turbines Power* **139** 031902
[15] Liu Z and Paniagua G 2017 *J. Eng. Gas Turbines Power* **140** 011601
[16] Grimshaw S D and Taylor J V 2017 Fast settling millimetre-scale five-hole probes *ASME Turbo Expo 2016* pp 1–13
[17] Börner M, Bitter M and Niehuis R 2018 *Journal of the Global Power and Propulsion Society* **2**
[18] Börner M and Niehuis R 2018 Development of the additive manufactured miniaturized wedge probe optimized for 2d transonic wake flow measurements *24th Biannual Symposium on Measuring Techniques in Turbomachinery August (Prague, Czech Republic)*
[19] Schmid M J, Müller M S, Kuhnle B A, Bauer M W, Pongratz R and Altmikus A 2016 Fiber optic acoustic pressure sensor with high dynamic range and low noise *Proceedings of the ETC 2016-36th European Telemetry and Test Conference (Nürnberg)*
[20] Schmid M J, Kuhnle B A, Kienitz S U, Napierala C F, Scheit C, Altmikus A, Müller M S and Koch A W 2017 A fiber-optic sensor for measuring quasi-static and unsteady pressure on wind energy converters *4SMARTS-Symposium* (Aachen: Shaker Verlag) (https://www.shaker.de/de/content/catalogue/index.asp?lang=de&ID=8&ISBN=978-3-8440-5083-7)
[21] Gibson I, Rosen D and Stucker B 2015 *Additive Manufacturing Technologies* (New York, NY: Springer New York)
[22] Vectoflow GmbH 2019 Products & services (https://www.vectoflow.de/en/products/), accessed on 2019-01-07
[23] Bach E, Bohon M, Paschereit C O and Stathopoulos P 2018 Development of an instrumented guide vane set for rdc exhaust flow characterization *2018 Joint Propulsion Conference* (https://doi.org/10.2514/6.2018-4479)
[24] Tran A V, Zhang X and Zhu B 2018 *Sensors (Switzerland)* **18** 2023
[25] Hashemian H, Black C L and Farmer J P 1995 Assessment of fiber optic pressure sensors *U.S. Nuclear Regulatory Commission, NUREG/CR-6312*
[26] Hill G C, Melamud R, Declercq F E, Davenport A A, Chan I H, Hartwell P G and Pruitt B L 2007 *Sensors and Actuators, A: Physical* **138** 52–62
[27] Yu Q and Zhou X 2011 *Photonic Sens.* **1** 72–83
[28] Yin J, Liu T, Jiang J, Liu K, Wang S, Qin Z and Zou S 2014 *IEEE Photonics Technol. Lett.* **26** 2070–3
[29] LightFab GmbH 2019 Products & technology (https://www.lightfab.de/), accessed on 2019-06-04
[30] Johansen E S, Rediniotis O and Jones G 2001 *Transactions of the ASME* **123** 128–38
[31] Rediniotis O K and Vijayagopal R 1999 *AIAA J.* **37** 666–74
[32] Conlon M J, Wright A, Abo H M and Ella E 2017 Measuring large flow angles using non-nulling multi-hole pressure probes *ASME Turbo Expo 2017* 1–7
[33] Beale M H, Hagan M T and Demuth H B 2019 Deep Learning Toolbox—User's Guide, R2019a *Tech. Rep. MathWorks, Inc.*
[34] Hagan M T and Menhaj M B 1994 *IEEE Transactions on Neural Networks/a Publication of the IEEE Neural Networks Council* **5** 989–93
[35] Bergh H and Tijdeman H 1965 *NLR-TR F.238* 21
[36] Semaan R and Scholz P 2012 *Exp. Fluids* **53** 829–37
[37] Meggitt E 2018 *Datasheet Model 8507C-2* (Meggitt (Orange County), Inc.) (https://buy.endevco.com/ContentStore/MktgContent/Endevco/Datasheet/8507C_DS_082219.pdf)